arXiv:2303.02803v1 [physics.flu-dyn] 5 Mar 2023

The characteristics of the meandering effect in a stratified wake

Xinyi Huang[1]†, and Jia-Qi J. L. Li[1]

[1]Department of Mechanical Engineering, Penn State University, University park, PA, 16802, USA

(Received xx; revised xx; accepted xx)

The gradual suppression of the vertical motions and the emergence of large-scale horizontal structures are characteristics of a stratified wake flow. We isolate the resulting wake meandering from the stationary velocity, i.e., the velocity without meandering, by utilizing direct numerical simulations covering Reynolds numbers $Re_B = UD/\nu$ between $[10000, 50000]$ and Froude number $Fr_B = U_B/ND$ between $[2, 50]$ (U_B is the freestream velocity, D is the characteristic length scale, and N is the buoyancy frequency). The meandering range is growing in the horizontal direction as the wake width, but decreases in the vertical direction, opposite to the wake height. The meandering, especially in the horizontal direction, leads to the dispersion of the instantaneous velocity and layered flow structures. Thus, the mean velocity profile deviates from the assumption of two-dimensional self-similarity in the late wake. Due to the distortion of the mean velocity profile, the superposition of the meandering to the stationary velocity is non-trivial. The scaling of the width and the height transitions at different points, and the scaling of the velocity deficit is further more complicated. Through theoretical analysis, we obtain and verify the momentum flux equation. We can accurately measure the impact of the meandering on the scaling of the lengths, and also the scaling of the velocity deficit.

Key words: None

1. Introduction

Stratified flow is ubiquitous in nature, both in the atmosphere (Mahrt 1999) and in the ocean (Hopfinger 1987). The wake behind a bluff body in a stratified flow is a canonical case that attracts a lot of attention (Meunier *et al.* 2006; Lin & Pao 1979; Spedding *et al.* 1996; Pal *et al.* 2017). The wake exhibits multiple stages along the downstream developing direction, and rich physics has been observed in this process (Nidhan *et al.* 2021).

One of the most evident flow dynamics is the meandering of the turbulent wake, which refers to the large-scale motion observed in the wake of the bluff body (Yang & Sotiropoulos 2019). The meandering can be seen as a result of coherent structures in the turbulent flow. It originates from the instability behaviour found near the bluff body, where both the Kelvin-Helmholtz billows and the lee waves are observed (Xiang *et al.* 2017). The instability is especially evident in the high Reynolds number cases. This stage is usually named the near wake regime (NW). The dynamics in the NW regime are similar to the unstratified counterpart since the buoyancy is relatively weak (Smyth

† Email address for correspondence: xuh128@psu.edu

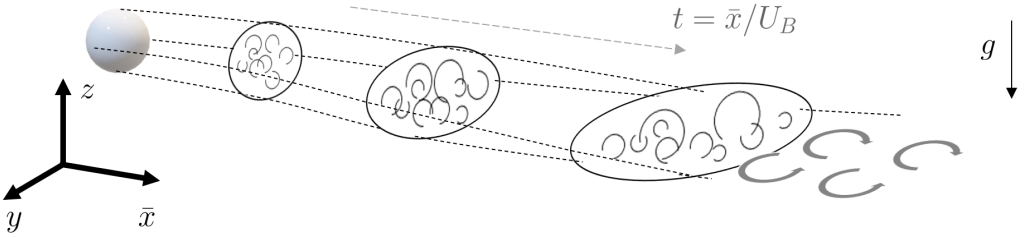

FIGURE 1. The sketch of a stratified wake behind a towed sphere. Several slices of the downstream locations are drafted, and the wake core is separated from the surrounding by the solid lines. The dash lines indicate the trajectory of the wake core boundary. The collapsed large-scale horizontal structures are formed at the late wake regime. We use $\bar{x}$ as the downstream location, y as the spanwise direction, and z for the vertical direction. The gravity is in the $-z$ direction. The temporal simulation is evolved in the $t = \bar{x}/U_B$ direction.

& Moum 2000). However, the NW regime is recognized to be short due to the growing buoyancy impact (Lin & Pao 1979).

Later on, the meandering starts to interact with the stratification. This stage is usually seen as the transition and is usually named the non-equilibrium regime (NEQ). In the NEQ regime, high Reynolds number cases still develop secondary instability events (Diamessis *et al.* 2011). Vortex structures interact with each other and are elongated in the streamwise direction after merging and straining (Spedding 2001). According to Smyth & Moum (2000), the smallest eddy size that is restrained from the buoyancy overturning decreases gradually. Therefore, the buoyancy effect grows relatively stronger and has a greater impact on the flow statistics. The vertical meandering is suppressed by the buoyancy, while the flow still grows in the horizontal direction, and thus the flow grows non-axisymmetric in its mean profile, and then further impacts the isotropy of the turbulence (Chongsiripinyo & Sarkar 2020).

In the end, the meandering is mainly in the horizontal direction. Large horizontal structures are formed since the buoyancy effect is strong enough to collapse the flow. The flow enters the stage named quasi-two-dimensional regime (Q2D), where the flow still has strong vertical shearing but has rather insignificant vertical velocities. There is little vertical transport, and vortices are decoupled into layers in the vertical direction (Basak & Sarkar 2006; Spedding *et al.* 1996). The horizontal motions constitute the majority of the kinetic energy (Spedding 2002*b*). The emergence of the large horizontal structures is universally seen in the stratified wake, regardless of the stratification strength (Spedding 1997).

We show the sketch of the stratified wake in figure 1. In this paper, we examine the flow over a towed sphere in a uniformly stratified environment, where the characteristic velocity is the towing speed U_B, and the characteristic length is the diameter of the sphere D. The global Reynolds number is $Re_B = U_B D/\nu$, where ν is the kinematic viscosity. The global Froude number is $Fr_B = U_B/ND$, where the Brunt-Väisälä frequency $N \equiv \sqrt{-\frac{g}{\rho_0}\frac{\partial \bar{\rho}}{\partial z}} = \sqrt{\frac{g}{T_0}\frac{\partial \bar{T}}{\partial z}}$ is the reciprocal of the buoyancy time scale, which indicates the strength of the background temperature gradient. Here, ρ_0, T_0 are the characteristic fluid density and fluid temperature, and $\frac{\partial \bar{\rho}}{\partial z}, \frac{\partial \bar{T}}{\partial z}$ are the background density gradient and the background temperature gradient. Therefore, Re_B and Fr_B are the control parameters for the stratified wake, where Re_B indicates the initial ratio between the inertia and the viscous force, and Fr_B indicates the initial ratio between the inertia and the buoyancy. However, the relative strength of the viscous force, the buoyancy and the inertia are not constant throughout the wake. The velocity deficit U_0 is decaying, while

the local horizontal wake size W is growing as sketched, leading to a decreasing local horizontal Froude number $Fr_H = U_0/WN$. This also explains why the flow is multi-stage (de Bruyn Kops & Riley 2019). We illustrate this multi-stage process in the sketch, and the wake core confined by the solid lines collapses in the Q2D regime, and finally forms the large-scale horizontal structures.

Multiple observed flow dynamics contribute to the energy transfer in the flow. Here, we would like to summarize a few of them. Firstly, Spedding (1997) verified the universal existence of the NEQ regime for a wide range of Fr_B. The energy transfer from the potential energy to the kinetic energy leads to a reduced decay rate in U_0, and thus prolongs the wake NEQ regime (Pal *et al.* 2017). Secondly, the internal gravity wave emerges in the stratified wake, and exchanges energy between the wake core and the surroundings. In Rowe *et al.* (2020), further examination of the internal gravity wave energy emission was carried out, and the internal gravity wave is found to be energetic in the NEQ regime. Also, the vertical layering of the vorticity patches leads to the high vertical shearing in the late wake, which is the most responsible component for the kinetic energy dissipation (Spedding 2002*b*). However, the energy transfer does not help to quantify the scaling laws of the flow statistics so far.

In the past decades, some theoretical analyses of the wake flow emerge due to the increased understanding of the flow dynamics. In the unstratified flow, Pope (2000) shows evidence of self-similarity and constant spreading rate in the experiments of the axisymmetric wake. Based on these observations, the traditional $-2/3$ law of the velocity deficit decay is derived out of the momentum conservation law. Therefore, the deficit velocity scaling in a stratified wake is similar to its unstratified counterpart for the NW regime (Brucker & Sarkar 2010). In the stratified flow, the self-similarity assumption and the omission of many other flow dynamics will give a complete set of scaling laws in multiple stages (Meunier *et al.* 2006). However, there is still no agreed universal power law in either mean flow or turbulence (Diamessis *et al.* 2011; Chongsiripinyo & Sarkar 2020). This may be because the intricacy in the flow dynamics breaks the assumptions. In the NW regime, the nonequilibrium turbulence dissipation effect requires modification to the traditional $-2/3$ law (Nedić *et al.* 2013). In the far wake, the self-similarity behaviour converges at a fairly late stage, especially in the higher-order statistics (Spedding 2001). The limited literature that verifies the self-similarity behaviour mainly focuses on the centre lines (Spedding *et al.* 1996; Spedding 2001).

As one of those important flow dynamics, the meandering effect is embedded throughout the flow development and becomes significant in the late wake. In the wake of wind turbines, the meandering effect impacts the wake recovery rate and the turbine load (Yang & Sotiropoulos 2019). Models for meandering have been developed to incorporate the meandering effect (Keck *et al.* 2014). However, the meandering effect is by far not much studied in the stratified wake of other bluff bodies, though it has been widely observed especially in the Q2D regime (Lin & Pao 1979).

In this paper, we study the meandering effect by isolating it from the stationary velocity, i.e., the velocity without meandering. We extract the centre location and the length scales of the instantaneous flow field and examine how they develop and how the control parameters Re_B and Fr_B change their behaviour. The mean velocity profile is thus the superposition of the meandering effect to the stationary velocity profile. A similar idea is proposed for the turbulent boundary layer (Krug *et al.* 2017), where the wake profile for a boundary layer can be modelled as a blending of the free stream and the log layer with a fluctuating interface. In Li *et al.* (2021), the blending is further extended to a rough-to-smooth transition in the turbulent boundary layer, where both the velocity profile and the streamwise turbulent intensity show excellent collapse with the

experimental data. However, there are non-trivial differences when applying the blending method to the stratified wake. The existence of gravity leads to the destruction of the axisymmetry. The anisotropy results in a two-dimensional velocity profile, and makes it more complicated than the one-dimensional blending in the boundary layer. The self-similarity in the unstratified wake theory might also be impacted (Pope 2000). On the other hand, the centre location can be explicitly extracted for each instantaneous velocity profile. This is in contrast to the turbulent boundary layer, where the flapping interface currently cannot be fully explained by the turbulent/non-turbulent interface (Krug *et al.* 2017).

The paper is organized as follows. In Sec. 2, We explain the extraction of the wake meandering characteristics, and develop the theoretical analyses on the superposition of the meandering to the stationary profile based on the two-dimensional self-similarity assumption. We elaborate our simulation details and case setup in Sec. 3. Then, we show the results of the meandering effect in Sec. 4, where we examine the self-similarity assumption, the development of the meandering properties, and the embedded flow structures out of conditional averaging. Lastly, the paper is concluded in Sec. 5.

2. Wake model with meandering

In a stratified wake, large-scale horizontal structures in the late wake have been observed in both the experiments (Lin & Pao 1979) and the simulations (Diamessis *et al.* 2011). Therefore, meandering is universal and shall be significant in the late wake.

To understand the meandering effect, we will extract the characteristic quantities out of the simulation data. We also compare the flow profiles with and without the meandering effect, which sheds light on how meandering alters the flow statistics. Next, we will develop the theory of the superposition of the meandering effect based on self-similarity assumptions. To the best of the authors' knowledge, this is the first attempt to systematically quantify the meandering effect and its corresponding impact on the scaling of the statistics in the stratified wake.

2.1. *Wake centre and length scales*

For every downstream location $\bar{x}/D$, the instantaneous velocity deficit is $u(y,z,t)$, where $\bar{x}$, y and z indicates the streamwise, the spanwise and the vertical direction. Here, t is the equivalent time in the temporal simulation for the downstream location $\bar{x} = U_B t$, and the nondimensional time $Nt = Fr_B^{-1} \cdot \bar{x}/D$. We illustrate this coordinate conversion in figure 1. Due to the stratification, the spreading of the wake size is not of the same rate in the y and z directions. To characterize the wake size, we need to find both the centre location y_c, z_c and the width and height W, H, where we use the subscript c to indicate the centre.

We follow a generalized way to identify the wake lengths W, H, by employing the second central spatial moment of the squared instantaneous velocity deficit (Brucker & Sarkar 2010). The centre location for $u(y,z,t)$ is therefore defined by

$$y_c(t) = \frac{\int_A y u(y,z,t)^2 \mathrm{d}A}{\int_A u(y,z,t)^2 \mathrm{d}A}, \quad z_c(t) = \frac{\int_A z u(y,z,t)^2 \mathrm{d}A}{\int_A u(y,z,t)^2 \mathrm{d}A}. \tag{2.1}$$

The length scales are computed by

$$W(t)^2 = C_0 \frac{\int_A (y-y_c)^2 u(y,z,t)^2 dA}{\int_A u(y,z,t)^2 dA}, \quad H(t)^2 = C_0 \frac{\int_A (z-z_c)^2 u(y,z,t)^2 dA}{\int_A u(y,z,t)^2 dA}. \tag{2.2}$$

Here, both of them are integrated through the cross-section A which excludes the sponge layer applied in the simulations. We use C_0 to guarantee consistency with the diameter definition. The initial mean profile is Gaussian, and we find that $C_0 = 2$ will guarantee $W(0) = H(0) = D/2$ during the initialization.

Therefore, we are able to extract the centre location and the length scales for all instantaneous snapshots however chaotic they are. The same technique can be applied to any other profiles we are interested in, as long as we substitute the instantaneous velocity deficit $u(y, z, t)$ by the corresponding quantities. For example, we may calculate the centre location and the length scales for the mean velocity profile $\overline{U}(y, z, t) = \langle u(y, z, t)\rangle$, where $\langle\cdot\rangle$ represents the ensemble average of the quantity. According to the symmetry, we should have $y_c = 0$ and $z_c = 0$ for $\overline{U}(y, z, t)$. However, note that the characteristic quantities of the mean profile are not necessarily the same as the mean of the instantaneous characteristic quantities.

2.2. *Superposition of the meandering effect*

All instantaneous velocity profiles can be seen as the superposition of the meandering effect and a stationary velocity profile whose centre is located at the mean wake centre. In this section, we will give some statistical analysis of the meandering effect, and no presumptions about the shape is made at the current stage. The symmetry of the sphere wake guarantees the mean wake centre at the domain centre through the wake development, which helps simplify the expressions, though it is not required in the analysis. For any instantaneous velocity profile centreed at (y_c, z_c), the stationary velocity profile is defined as $u_s(y, z, t) = u(y+y_c, z+z_c, t)$. We are able to find the mean stationary profile by

$$\overline{U}_s(y, z, t) = \langle u_s(y, z, t)\rangle = \langle u(y + y_c, z + z_c, t)\rangle. \tag{2.3}$$

We are also able to obtain the conditional stationary profile with the centre location (y_c, z_c) by conditional averaging, i.e.,

$$U_s(y, z, y_c, z_c, t) = \langle u_s(y, z, t)\rangle|_{|y_{c0}-y_c|/D<\Delta_s, |z_{c0}-z_c|/D<\Delta_s}. \tag{2.4}$$

Here, Δ_s is the averaging window, and the instantaneous snapshots with the centre location (y_{c0}, z_{c0}) falling in the averaging window will be used for calculation. We choose $\Delta_s = 0.1$ out of the rule of thumb. The mean stationary profile $\overline{U}_s(y, z, t)$ is the collapse of the conditional stationary profile $U_s(y, z, y_c, z_c, t)$ by averaging out for various centre locations. Correspondingly, the mean velocity profile with meandering $\overline{U}(y, z, t)$ is therefore the collapse of the meandered conditional profile by averaging out for various centre locations. To be exact,

$$\overline{U}_s(y, z, t) = \iint U_s(y, z, y_c, z_c, t)p_c(y_c, z_c, t)\mathrm{d}y_c\mathrm{d}z_c, \tag{2.5}$$

$$\overline{U}(y, z, t) = \iint U_s(y - y_c, z - z_c, y_c, z_c, t)p_c(y_c, z_c, t)\mathrm{d}y_c\mathrm{d}z_c. \tag{2.6}$$

Here, $p_c(y_c, z_c, t)$ is the joint probability density function (p.d.f.) of the centre location. These equations can be obtained through the definitions of the conditional average and the ensemble average (Antonia 1981).

2.3. *Self-similarity assumptions and simplifications*

Next, we would like to discuss the possible self-similarity assumptions. The superposition equations of the meandering can thus be simplified, which helps spot the meandering effect in the scaling of the statistics.

If we assume that the self-similarity for the mean velocity profile preserves till the late wake, we have a universal expression for the velocity profile after a coordinate transformation,

$$\overline{U}(y,z,t) = \hat{U}(\xi,\eta,t) = U_0(t)f(\xi,\eta), \quad \text{where } \xi = y/W,\ \eta = z/H. \tag{2.7}$$

We use the subscript 0 to denote the centre velocity deficit, and W and H are the width and height for $\overline{U}(y,z,t)$ calculated as in Sec. 2.1.

To separate the meandering effect from the stationary profile, we further assume self-similarity in the conditional stationary profiles $U_s(y,z,y_c,z_c,t)$ and the joint p.d.f. of the centre location $p_c(y_c,z_c,t)$ throughout the downstream locations. As for the conditional stationary profiles, the self-similarity is as follows,

$$\begin{aligned} U_s(y,z,y_c,z_c,t) &= \hat{U}_s(\xi_s,\eta_s,\xi_{sc},\eta_{sc},t) = U_{s0}(t)g(\xi_s,\eta_s), \\ &\text{where } \xi_s = y/W_s,\ \eta_s = z/H_s,\ \xi_{sc} = y_c/W_s,\ \eta_{sc} = z_c/H_s. \end{aligned} \tag{2.8}$$

The subscript s represents the stationary velocity, and W_s and H_s are the width and height of the stationary profile. As for the joint p.d.f. of the centre location, the self-similarity is as follows,

$$p_c(y_c,z_c,t) = \hat{p}_c(\xi_{pc},\eta_{pc})p_{c0}(t), \quad \text{where } \xi_{pc} = y_c/W_p,\ \eta_{pc} = z_c/H_p, \tag{2.9}$$

where the subscript p represents the p.d.f. of the centre location, and $p_{c0}(t)$ is the normalization term such that the integration of the joint p.d.f. across the wake cross-section is 1 before and after the coordinate transformation, i.e.,

$$\iint \hat{p}_c(\xi_{pc},\eta_{pc})\mathrm{d}\xi_{pc}\mathrm{d}\eta_{pc} = 1. \tag{2.10}$$

Now, we can express the velocity deficit $\overline{U}(y,z,t)$ as the combination of the velocity deficit amplitude $U_{s0}(t)$ for the conditional stationary profile and the self-similar profiles. The simplification of the superposition equation (2.6) is

$$\overline{U}(y,z,t) = U_{s0}(t)\iint g(\xi_s-\xi_{sc},\eta_s-\eta_{sc})\hat{p}_c(\xi_{pc},\eta_{pc})\mathrm{d}\xi_{pc}\mathrm{d}\eta_{pc}. \tag{2.11}$$

Note that this does not necessarily require the same length scales of the p.d.f. as those of the mean velocity profile. The change of the length scales will lead to the change of the value in the integral, which is a function of t.

Thus, we are able to link the centreline deficit velocities $U_0(t)$ and $U_{s0}(t)$ by

$$U_0(t) = U_{s0}(t)\iint g(\xi_{sc},\eta_{sc})\hat{p}_c(\xi_{pc},\eta_{pc})\mathrm{d}\xi_{pc}\mathrm{d}\eta_{pc}. \tag{2.12}$$

It always stands that $U_0(t) \leqslant U_{s0}(t)$ since $g \leqslant 1$, so the meandering effect will reduce the mean velocity deficit.

The centreline velocity deficit therefore collapses to be

$$\begin{aligned} U_0(t) &= C_s(t)U_{s0}(t), \\ \text{where } C_s(t) &= \iint g(\xi_{sc},\eta_{sc})\hat{p}_c(\xi_{pc},\eta_{pc})\mathrm{d}\xi_{pc}\mathrm{d}\eta_{pc}. \end{aligned} \tag{2.13}$$

If the proportional relationship between W, H and W_p, H_p keeps constant as flow develops, we will obtain $C_s(t) = \text{const}$. Therefore, the meandering will lead to a reduction in the mean velocity deficit U_0, and may impact its scaling as the characteristic lengths change.

Intuitively, $p_c(y_c, z_c, t)$, as the possibility of the meandering location (y_c, z_c), is the quantification of the mean meandering behaviour. We know that the centre location $y_{cp} = 0$ and $z_{cp} = 0$ due to the symmetry. We can also extract the width and height of the p.d.f., W_p, H_p. They are the measurement of the range of the meandering in the horizontal and the vertical directions. A large W_p is expected in the late wake regime, since the large-scale structures will be formed in the stratified environment through vortex interactions and the instantaneous horizontal centre location is expected to vary greatly.

Up till now, only self-similarity is assumed. If we further assume that g and $\hat{p}_c$ are standard 2D Gaussian distributions, the convolution will bring that f is also 2D Gaussian distributed, and that the superposed length scales follow

$$W_{sp}^2 = W_s^2 + W_p^2, H_{sp}^2 = H_s^2 + H_p^2. \tag{2.14}$$

To evaluate the variation in the instantaneous profiles, we may also study the p.d.f. of the wake length scales $p_l(W, H, t)$, where the subscript l indicates the length scales. Intuitively, $p_l(W, H, t)$, as the possibility of a specific pair of (W, H), indicates the possible distortion of the instantaneous velocity. If we have a large span of $p_l(W, H, t)$ in space, the instantaneous velocity varies strongly in its profile. To sum up, both joint p.d.f. profiles are the quantification of the meandering behaviour.

2.4. *Momentum flux equation*

Here, we would like to build the connection between the scaling of the velocity and the scaling of the lengths. We start with the momentum conservation law (Pope 2000; Tennekes *et al.* 1972), which says

$$\iint \rho \overline{U}(U_B - \overline{U}) \mathrm{d}y\mathrm{d}z = \text{const}, \tag{2.15}$$

where U_B is the tow speed, i.e., the free stream velocity. If we only consider flow far downstream that the velocity deficit is weak compared to the tow speed, i.e., $\overline{U} \ll U_B$, we are able to simplify the momentum conservation law to

$$\iint \overline{U}(y, z, t) \mathrm{d}y\mathrm{d}z = \text{const}. \tag{2.16}$$

The constant indicates the momentum flux along the streamwise direction, and it remains constant. Based on the self-similarity assumption of the mean velocity, we may therefore reduce equation (2.16) to

$$\iint \overline{U}(y, z, t) \mathrm{d}y\mathrm{d}z = U_0(t) W(t) H(t) \iint f(\xi, \eta) \mathrm{d}\xi\mathrm{d}\eta = \text{const}, \tag{2.17}$$

i.e.,

$$U_0(t) W(t) H(t) = M(t) U_B D^2, \tag{2.18}$$

where $M(t) = M_0$ shall be a nondimensional constant for the conservation law of the momentum flux. Note that the simplified conservation law does not require the exact expression of the self-similar profile. It stands as long as self-similarity exists for the velocity profile with a weak velocity deficit.

Similarly, we apply the momentum conservation to the mean stationary profile $\overline{U}_s(y, z, t)$ based on the self-similarity equation (2.8) and obtain the same simplified equation for U_{s0} and W_s, H_s,

$$U_{s0}(t) W_s(t) H_s(t) = M_s(t) U_B D^2, \tag{2.19}$$

Case	Sym.	Re_B	Fr_B	L_x	L_y	L_z	N_x	N_y	N_z	t_f	Rep.
R10F02	◀	10,000	2	60	38	14	1280	768	256	1380.18	100
R20F02[1]	▲	20,000	2	60	24	12	1280	768	384	109.29	100
R20F02[2]	▲	20,000	2	60	36	12	1280	576	192	800.62	100
R20F10[1]	●	20,000	10	60	24	12	1280	768	384	109.29	80
R20F10[2]	●	20,000	10	60	36	12	1280	576	192	1220.58	80
R20F50[1]	▼	20,000	50	60	24	12	1280	768	384	109.29	80
R20F50[2]	▼	20,000	50	60	36	12	1280	576	192	568.91	80
R20F50[3]	▼	20,000	50	60	48	24	640	384	192	5232.38	80
R50F50[1]	▶	50,000	50	60	8.25	8.25	2560	550	550	67.46	80
R50F50[2]	▶	50,000	50	60	23.04	11.52	1280	768	384	265.72	80
R50F50[3]	▶	50,000	50	60	46.08	23.04	640	512	256	5800.23	80

TABLE 1. Details of the 440 DNS cases carried out. We use 'R[Re_B/1000]F[Fr_B]' to differentiate between cases with different bulk Reynolds numbers Re_B, and bulk Froude numbers Fr_B. Thecolour and the symbol type for each case are given in 'Sym.'. The five cases are regridded at different t_f, and the period of regridding is indicated by its superscript. The multiple periods of each case share the same symbol. Note t_f is the equivalent end time of the temporal simulation to the downstream location from the body. The simulations are each independently repeated for either 80 or 100 times, given by the column 'Rep'. The temporal simulations are homogeneous in the x direction, and the ensemble average can be carried out for both the streamwise direction and for multiple cases.

where $M_s(t) = M_{s0}$ shall also be a constant through time according to the conservation law.

We know that the flow deficit decays fast downstream. Exceptions are mainly in the near wake regime for low Fr case (Pal *et al.* 2017). Therefore, the conservation of the momentum flux is guaranteed in the late wake when the self-similarity assumptions stand.

3. Simulation details

We conduct direct numerical simulations of the wake behind a towed sphere in a stably stratified flow, where the background temperature gradient is $\partial\overline{T}/\partial z$. Five cases with different flow control parameters are examined for $\mathcal{O}(100)$ repetitions, and we therefore can obtain ensemble-averaged flow fields. Following de Stadler *et al.* (2010), we employ the temporally evolving framework in order to obtain far wake statistics, which has been utilized and verified in many literatures (Gourlay *et al.* 2001; de Stadler & Sarkar 2012; Zhou & Diamessis 2016). The flow evolves downstream in the reference frame fixed with the free stream, and is set periodic in the streamwise direction (x) as the characteristic streamwise length scale is much longer than the other two directions. A sponge layer with thickness $L_{\text{sponge}}/D = 1$ is employed in the spanwise (y) and the vertical (z) directions to absorb the emitted internal gravity waves. We also have periodicity in the y and z directions.

The simulations are independently and randomly initiated for all the repetitions. The initialization is some distance behind the sphere to avoid the recirculation regime. As Brucker & Sarkar (2010), the synthesized initial velocity fields keep the same mean velocity profile and the turbulent kinetic energy measured from the experiments. Therefore, these initial profiles determine that the momentum flux constants $M_0 = 0.0275$ and $M_{s0} = 0.0267$. The velocity fluctuations are created in the spectral space to ensure an initial broadband energy spectrum, and are exponentially damped along the radial direction. The mean velocity and the turbulent kinetic energy profiles are held the same

to develop the correlation between the mean and the fluctuation for turbulent wake (Dommermuth *et al.* 2002). We gradually impose the gravity field between $t = 6$ and $t = 8$ to include the buoyancy effect. We refer the readers to Dommermuth *et al.* (2002) and de Stadler *et al.* (2010) for more details of the simulations.

We use an in-house second-order finite-difference solver, which has been verified (Yang *et al.* 2020, 2015; Li & Yang 2021), to solve the incompressible Navier-Stokes equations. We employ the Boussinesq approximation, and the buoyancy effect is included as a body force in the momentum equations. All the quantities are normalized using D, U_B and $\partial\overline{T}/\partial z$. The pressure Poisson equation is solved to ensure incompressibility. The flow is advanced using the third-order Runge-Kutta time scheme.

The flow control parameters are the global Reynolds number Re_B and the global Froude number Fr_B. We list the details of the five cases in Table 1, where "R$[Re_B/1000]$F$[Fr_B]$" denotes Re_B and Fr_B. The high Reynolds number cases have a larger wake size and a decreasing local Reynolds number downstream, i.e., the Kolmogorov scale $\eta = (\nu^3/\varepsilon)^{1/4}$ gradually increases. We regrid the flow field and enlarge the computational domain at the temporal time step $t = t_f$, when we still ensure $\Delta x_i/\eta < 2 \sim 4$ as required by Kim *et al.* (1987). The cases R20F02 and R20F10 have been regridded once, while the cases R20F50 and R50F50 have been regridded twice. Therefore, all the cases are run till the Q2D regime, which leads to a big t_f for high Re_B and high Fr_B cases.

Each case is independently repeated 80 or 100 times to ensure the convergence in the pre-multiplied p.d.f. of all the first and the second order statistics. The ensemble-averaged quantities are obtained by the combination of streamwise averaging and averaging among the independent repetitions. This is because of the homogeneity in the streamwise direction and the random initialization. To quantify the meandering behaviour, the centre location and the width and height are extracted for all the streamwise slices for all the repetitions. We will study the joint probability density function (p.d.f.) of the wake centre location $p_c(y_c, z_c, t)$ and it requires a huge amount of ensemble data to converge. We use kernel density estimation to obtain p.d.f. from large data samples (Botev *et al.* 2010).

4. Results

4.1. *Visualization*

We first visualize the meandering of a stratified turbulent wake in the instantaneous flow fields. Figures 2 and 3 are both from the case R20F02, and they show typical vortical structures in the NEQ regime and in the Q2D regime respectively. In the NEQ regime, asymmetric structures with vertical vorticity ω_z of opposite signs are densely packed along the centreline, and shed downstream. The turbulent flow in the wake core is composed of fine turbulent eddies of multiple scales. We pick two locations where we observe strong meandering behaviour along the y direction, and show the corresponding instantaneous streamwise velocity u/U_B in the $y-z$ planes. At both locations, the wake core is more stretched in the horizontal direction than in the vertical direction because of the stratification. Also, the meandering behaviour is stronger in the horizontal direction. In the Q2D regime, the vortical structures are larger in the horizontal direction and they are more isolated from each other due to the pairing and merging of the wake cores (Spedding 2002*a*; Basak & Sarkar 2006). Fine-scale structures are less visible in the turbulent flow compared to the NEQ regime, and there are no internal gravity waves. In the meantime, the horizontal meandering grows larger with the horizontal length scale, while the vertical meandering is still relatively minimal.

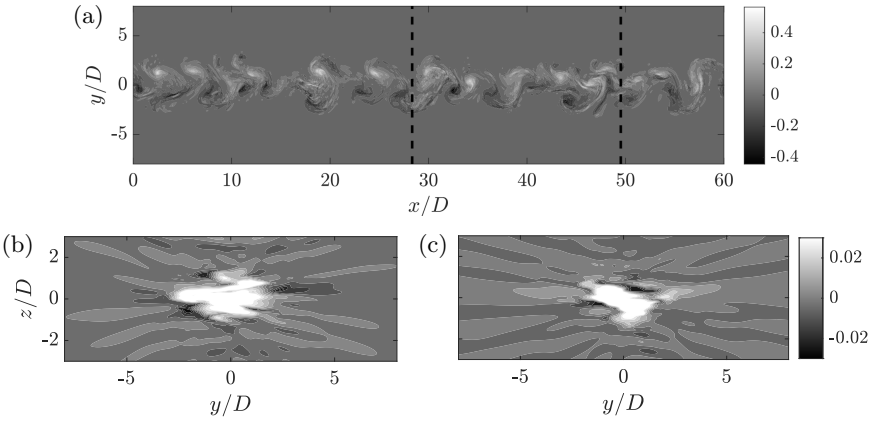

FIGURE 2. The instantaneous flow fields for R20F02 at $Nt = 45.6$, which falls in the NEQ regime. (a) The normalized vertical vorticity $\omega_z D/U_B$ in the $x - y$ plane at the wake centre. (b,c) The normalized streamwise velocity u/U_B in the $y - z$ plane extracted at (b) $x/D = 28.3$ and (c) $x/D = 49.5$, denoted by the black dashed lines in (a). The visualization is limited to $-8 < y/D < 8$ and $-3 < z/D < 3$ for clarity.

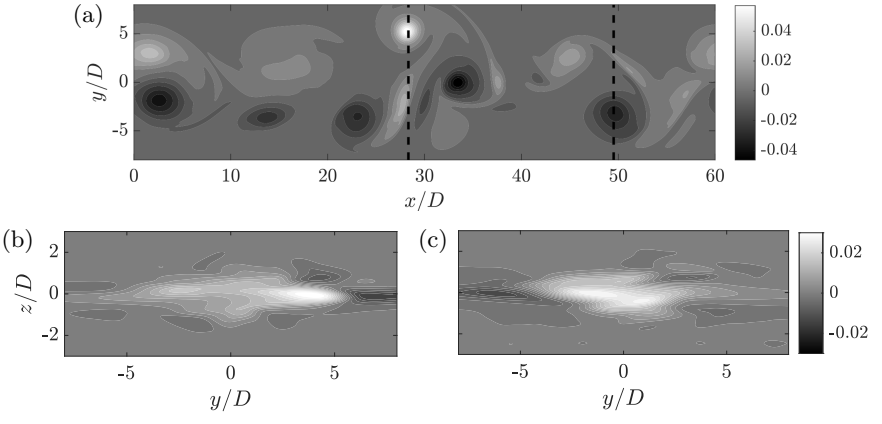

FIGURE 3. The instantaneous flow fields for R20F02 at $Nt = 400.3$, which falls in the Q2D regime. The contour settings are the same as figure 2.

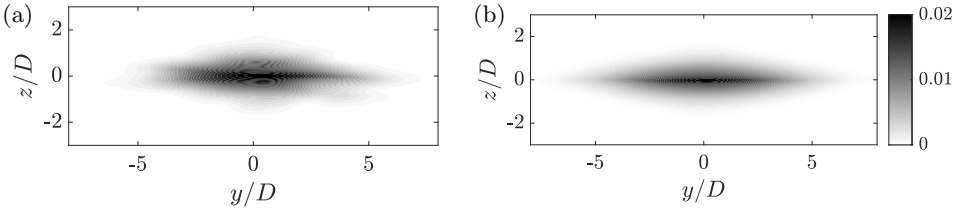

FIGURE 4. The comparison of the mean velocity in the $y-z$ plane between (a) the 100-repetition ensemble average and (b) the 1-repetition ensemble average. They are both from the case R20F02 at $Nt = 400.3$.

We obtain the statistics through ensemble averaging. In temporal simulations, the statistics are traditionally the streamwise average due to the homogeneity in the streamwise direction (Gourlay *et al.* 2001; de Stadler & Sarkar 2012; Rowe *et al.* 2020). However, only using the streamwise average is not enough to obtain a converged velocity profile as is shown in figure 4 (a), which falls in the Q2D regime and we may exclude the influence

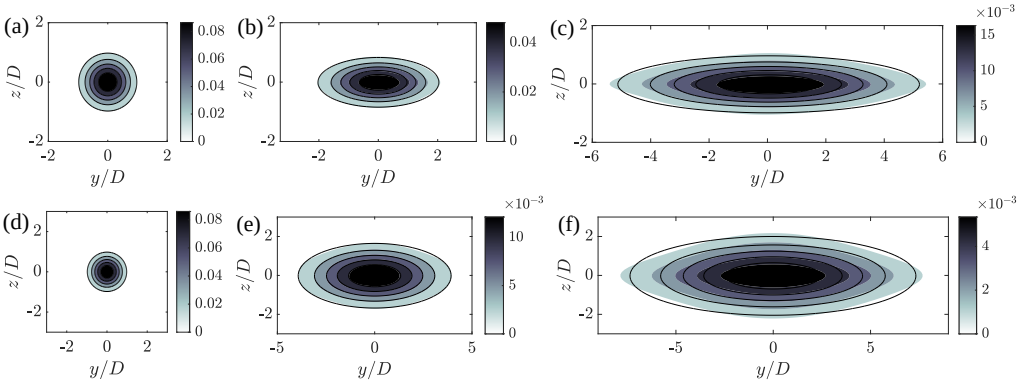

FIGURE 5. The mean velocity field $\overline{U}(y,z,t)$ in the $y-z$ plane for (a,b,c) R20F02 and (d,e,f) R20F50. The solid lines are the same contour levels from the 2D Gaussian fit of $\overline{U}$. The examined time steps are (a) $Nt = 4.1$, (b) $Nt = 45.6$, (c) $Nt = 400.3$ in R20F02 and (d) $Nt = 0.2$, (e) $Nt = 18.6$, (f) $Nt = 104.6$ in R20F50. Note that the contours have different axis limits due to the change in the wake core size.

of the internal gravity. The boundary of the wake core is oscillatory, which indicates the insufficiency of the sampling when the averaging is from only 1 repetition. In our calculation, we initialize each case independently 80 or 100 times, and the ensemble average is the average both in the streamwise direction and among the independent repetitions. The 100-repetition ensemble average in figure 4 (b) show better convergence, and the improvement happens to other time steps and other cases we work with, especially in the Q2D regime where the horizontal meandering is large.

4.2. *Two-dimensional self-similarity*

We now examine the self-similarity assumption of the mean velocity profiles $\overline{U}(y,z,t)$. The self-similarity assumption is usually examined in one-dimension along y- and z-centerlines (Spedding *et al.* 1996). The normalized 1D profiles are close to the Gaussian function, and the z-centerline profile has a thicker tail than the y-centerline profile in the late wake (Spedding 2001). The anisotropy in the y- and z-directions further indicates the possibility of distortion in the velocity profiles. In figure 5, we compare the mean velocity field in the $y-z$ plane and their 2D least-square Gaussian fit for all three regimes. Both cases R20F02 and R20F50 are expanding in the y-direction and are suppressed in the vertical motion. The characteristic vertical length is smaller for case R20F02 when the horizontal length is comparable, see figure 5 (c,f), since Fr_B is smaller, which means a stronger background stratification. The velocity profiles in both the NW and the NEQ regimes are close to Gaussian behaviour. However, we qualitatively see that the velocity profiles in the Q2D regime for both cases are distorted from the 2D Gaussian fit, while the wake core thickness in R20F50 is much larger than R20F02. This indicates that the differences in the flow dynamics among the three regimes have a stronger impact on the velocity profile, while the characteristic length scales are not directly related.

The normalized deviation from the Gaussian profile is negligible in the NW regime, and gradually grows to be relatively large in the Q2D regime as is shown in figure 6. In the NW regime and the NEQ regime, as in the first two columns, the deviations are small enough in the whole domain, the maximum absolute of which is 4.7%. In the Q2D regime, as in the third column, the maximum deviation from the Gaussian profile reaches 6.5%. The normalized areas of the large deviation, i.e., the absolute deviation is more

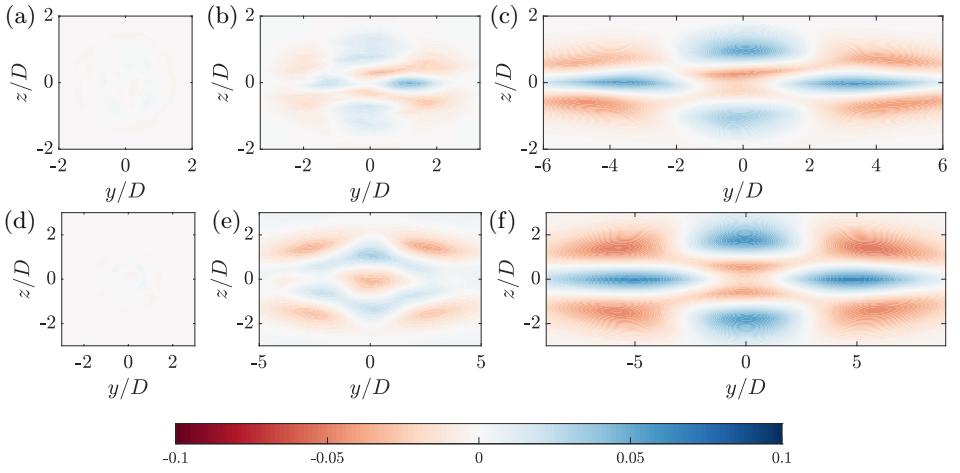

FIGURE 6. The difference between $\overline{U}(y,z,t)$ and its 2D Gaussian fit for the same time steps and cases as in figure 5. They fall respectively in the NW regime, the NEQ regime and the Q2D regime from left to right. All the profiles are normalized by the maximum value U_0 of the 2D Gaussian fit.

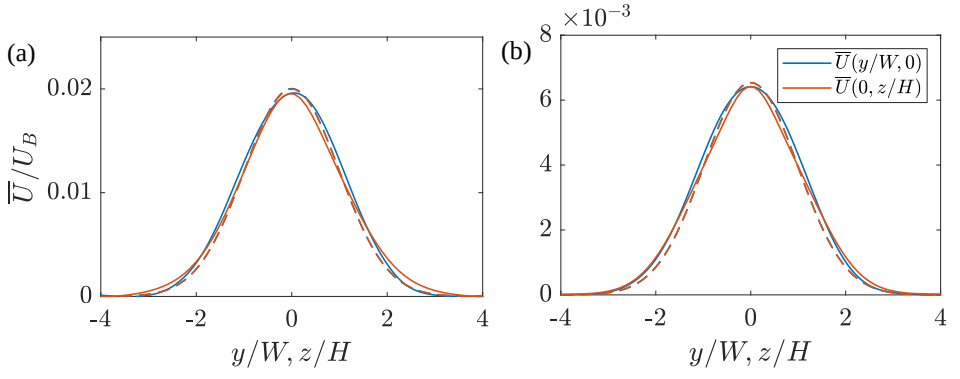

FIGURE 7. The velocity profiles $\overline{U}$ along the horizontal centreline $\overline{U}(y/W,0)$ and the vertical centreline $\overline{U}(0,z/H)$. The examined time steps are (a) $Nt = 400.3$ in R20F02 and (b) $Nt = 104.6$ in R20F50. We use the dashed lines to represent the extracted centreline profiles of the 2D Gaussian fit.

than 5.0%, are 0.58 and 4.50 in figures 6 (c,f) respectively, and these are comparable sizes to the whole wake core.

The pattern of the deviation is also noteworthy. In figure 7, we extract the horizontal centreline $\overline{U}(y/W,0)$ and the vertical certerline $\overline{U}(0,z/H)$, and compare the velocity profiles $\overline{U}$ and their 2D Gaussian fit. We observe that the centreline profiles are a bit fatter than the Gaussian profile, and the vertical profiles have a thicker tail in the NEQ regime, consistent with the observation of Spedding (2001). The positive areas observed near the centrelines of the deviation contours also indicate the fatter centreline profiles. Away from the centrelines, the areas are mainly negative, and this indicates thinner profiles. The diverging behaviour denies the possibility of a simple modification to the self-similar profile after local normalization that keeps the universality along the downstream direction. This indicates the existence of underlying flow dynamics that distorts self-similarity.

To further evaluate the contribution of the meandering, we examine the normalized

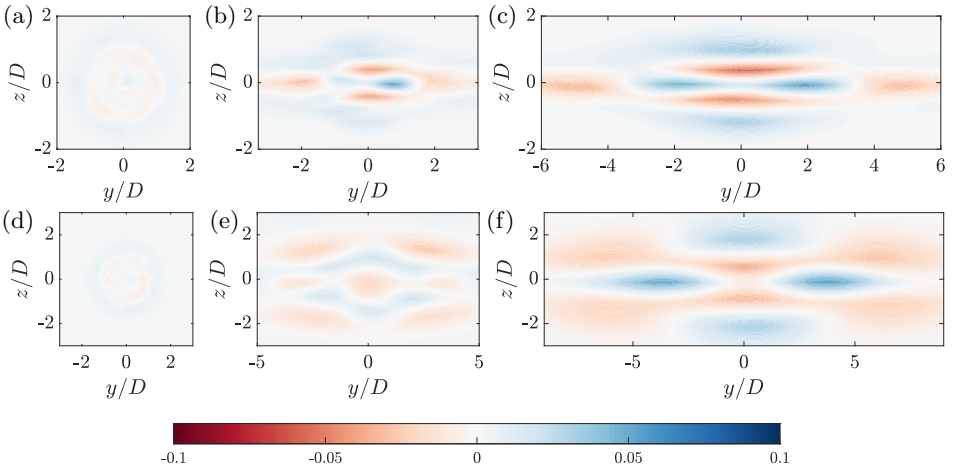

FIGURE 8. The difference between the mean stationary velocity profile $\overline{U}_s(y,z,t)$ and its Gaussian fit in the $y-z$ plane, normalized by the centre velocity deficit value U_0, at the same time steps and cases as in figure 5.

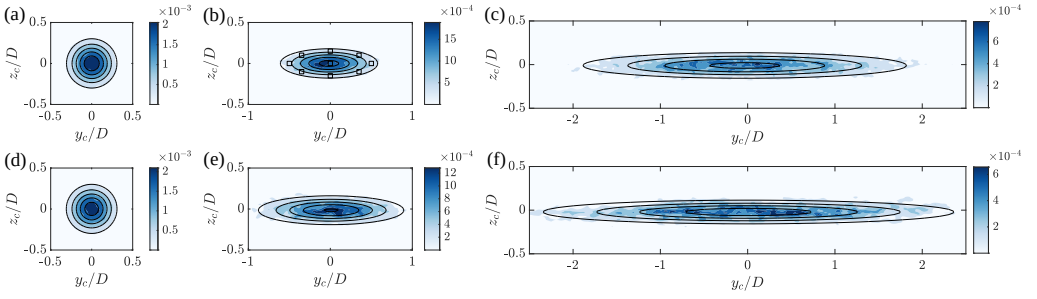

FIGURE 9. The joint p.d.f. of the instantaneous centre location (y_c, z_c) in the $y-z$ plane for (a,b,c) R20F02 and (d,e,f) R20F50. The solid lines are the same contour levels from the 2D Gaussian fit of the joint p.d.f. $p_c(y_c, z_c, t)$. The examined time steps are the same as figure 5. In (b), the blue squares are centre locations of the conditional stationary velocity profile $\overline{U}_s$ in figure 13.

deviation from the Gaussian profile of the mean stationary velocity $\overline{U}_s(y,z,t)$ in figure 8. We see a similar pattern of the growing distortion away from the Gaussian behaviour as in figure 6. The vertical centreline profiles still have a thicker tail than the horizontal centreline profiles. However, the general level of deviation is greatly reduced. In the Q2D regime, the maximum absolute value of the normalized deviation is 5.6%, and the areas of large deviation are reduced to 0.22 and 0.28 in figures 8 (c,f) respectively. The deviation is now qualitatively mainly restrained in the wake core after excluding the meandering effect. Therefore, the meandering effect, as the main difference between U and $\overline{U}_s$, is one major source of the distortion of self-similarity. We will further quantify the meandering behaviour in the following sections and evaluate its impact.

4.3. *Meandering behaviour*

Meandering is the large-scale movement in the wake. To quantify the meandering behaviour of the stratified wake, we extract the centre locations and the length scales of the instantaneous velocity profiles. We focus on the corresponding joint probability density functions, $p_c(y_c, z_c, t)$ and $p_l(W, H, t)$. The former reveals the range of the

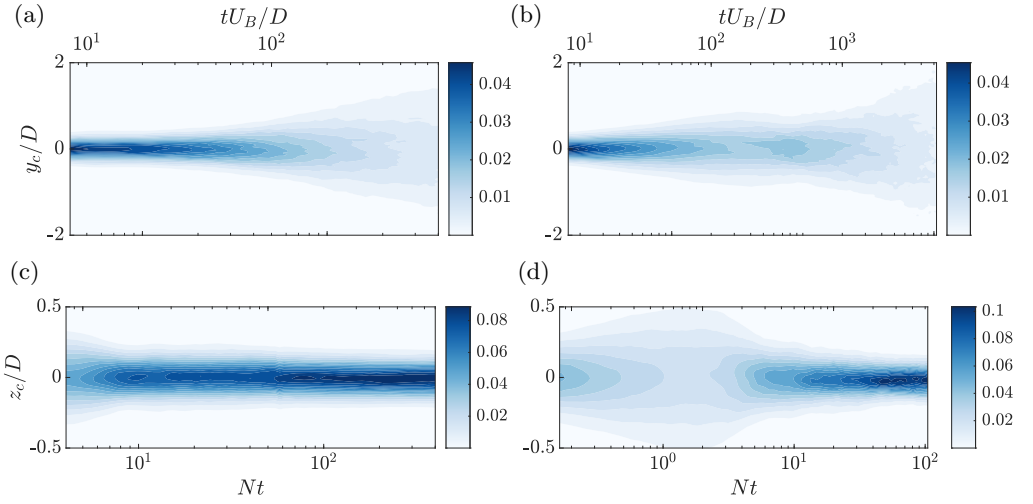

FIGURE 10. The development of the marginal p.d.f. of the centre location in (a,b) the y-direction $p_{c,Y}(y_c, t)$ and (c,d) in the z-direction $p_{c,Z}(z_c, t)$. The left column (a,c) are for the case R20F02, and the right column (b,d) are for the case R20F50.

meandering, and the latter measures the distortion of the velocity profile during the process of meandering.

In figure 9, the joint p.d.f. of the centre location $p_c(y_c, z_c, t)$ is close to a Gaussian function for a long range of time steps as examined. As the flow develops downstream, $p_c(y_c, z_c, t)$ is expanding fast in the horizontal direction, similar to the wake width W. This indicates a simultaneous horizontal expansion of the meandering with the widening stratified wake. However, the meandering gradually shrinks in the vertical direction, although the wake height H is maintained near a constant as shown in figure 5. The characteristic length scales of $p_c(y_c, z_c, t)$ for R20F02 are comparable to R20F50, regardless of the background stratification strength Fr_B. The case R20F50 has a slightly narrower vertical meandering while it has a slightly stronger horizontal meandering, as shown in figures 9 (c,f). We note that the range of both the horizontal and the vertical meandering is much smaller than the width and height of the wake core, and this will constrain the impact of the meandering.

The marginal p.d.f. profiles of the centre locations further visualize the development of the meandering range. In figure 10, the marginal p.d.f. profiles of the horizontal location $p_{c,Y}(y_c, t)$ and the vertical location $p_{c,Z}(z_c, t)$ are examined along the time direction, where the subscript Y or Z indicates the spatial marginal direction. The range of the horizontal meandering keeps growing through the wake, while the range of the vertical meandering collapses in the late wake. We observe roughly three stages out of the development of the meandering range in the cases. Note that they do not necessarily correspond to the NW regime, the NEQ regime and the Q2D regime. Before $Nt \sim 3$, both the horizontal and the vertical range of meandering are growing at a decaying rate. For R20F02, the background stratification is so strong that there is almost no such stage. When Nt is between $[3, 20]$, the horizontal range of meandering does not change much, while the vertical range of meandering gradually decreases. After $Nt \sim 20$, the meandering in the vertical direction is limited to a similar range for both R20F02 and R20F50, while the meandering in the horizontal direction still grows. However, there is no explicit criterion on when the transition exactly happens, and there is no guarantee

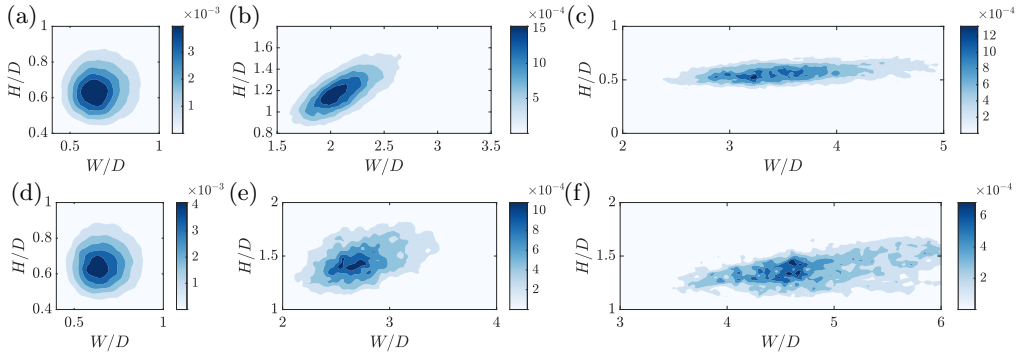

FIGURE 11. The joint p.d.f. of the instantaneous width and height (W, H) for the same cases and the same time steps as in figure 5.

that the horizontal and the vertical direction share the same transition points. A similar developing pattern of the meandering range is observed in other cases.

Figure 11 shows how the joint p.d.f. of the instantaneous width and height $p_l(W, H, t)$ changes through time. In the NW regime, both the width W and the height H span a wide range and they are comparable. They are positively correlated, though the correlation is not strong. In the NEQ regime, both W and H grow larger, though the width W is much larger than the height H. Both W and H span larger in distribution, though W varies in a wider range than H. The positive correlation grows stronger, and thus, an instantaneous velocity profile that expands in the horizontal direction possibly expands in the vertical direction. In the Q2D regime, the positive correlation is not that strong since the spanning of the wake height H grows narrower. In the meantime, the wake width W still has a wide span in p.d.f., which indicates a wide variation range in the wake shape.

In general, on one hand, we see a consistent developing process of the width and the height in the instantaneous velocity profiles with our observation of the mean velocity profiles. The width W keeps growing for both cases. The height H grows at the beginning, but maintains near a constant for a long time, and the constant is smaller for lower Fr_B due to the strong background stratification. On the other hand, the span of the width and the height in p.d.f., which is related to the variation of the wake shape, shares some similarities with the meandering. The width spans a larger range through the wake for both cases. The height also spans larger in the early wake, but the spanning range grows narrower in the late wake, which is similar to the late-wake vertical shrinkage of the meandering range.

The larger variation of the wake shape in the late wake is actually found to be related to the meandering behaviour. In figure 12, we examine the p.d.f. of the width when conditioned on a weak vertical meandering and on a strong vertical meandering under different situations. The conditional p.d.f.s have a similar range, shown by the blue lines, when the flow has not entered the late wake. Stronger background stratification will lead to another peak with a large width value in figure 12 (a), though. As the flow enters the late wake, the strong vertical meandering tends to increase the wake width. For R20F02, the wake width increases in all, while for R20F50, the p.d.f. obtains another peak near the tail. The deviation of the conditional p.d.f. indicates that the late wake meandering is a source of the wake profile distortion.

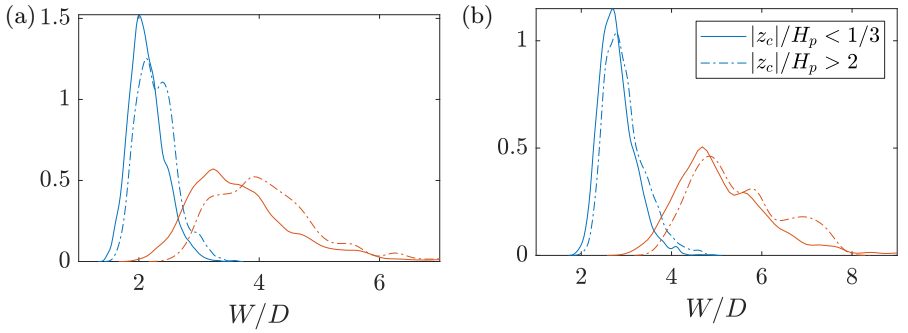

FIGURE 12. The p.d.f. of the instantaneous width conditioned on a weak vertical meandering, $|z_c|/H_p < 1/3$, given by the solid lines, and on a strong vertical meandering, $|z_c|/H_p > 2$, given by the dash-dotted lines. (a) Case R20F02. The blue lines are at $Nt = 45.6$, and the orange lines are at $Nt = 400.3$. (b) Case R20F50. The blue lines are at $Nt = 400.3$, and the orange lines are at $Nt = 104.6$.

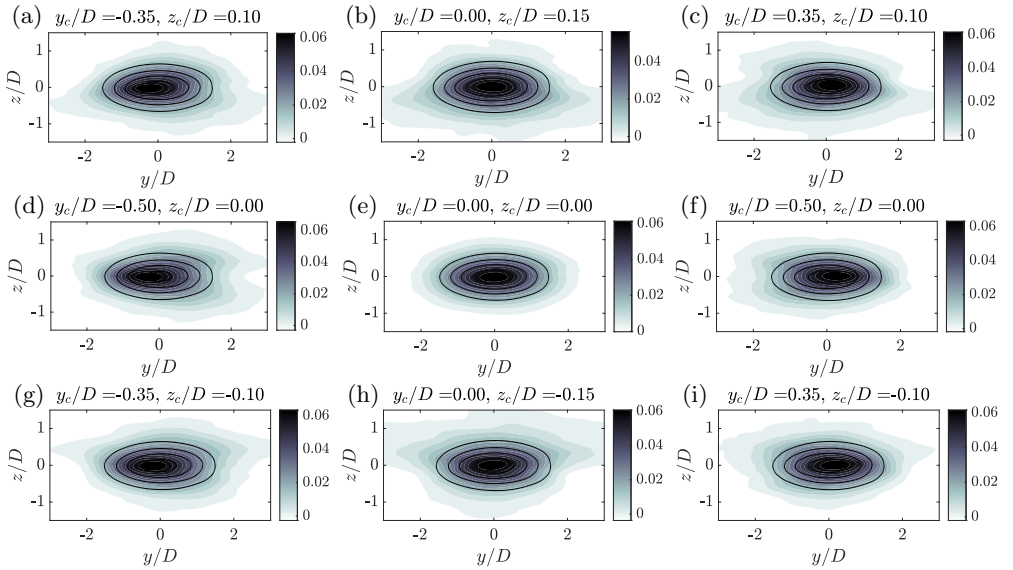

FIGURE 13. The conditional stationary velocity profile $U_s(y, z, y_c, z_c, t)$ conditionally averaged on the centre location (y_c, z_c). The time step is $Nt = 45.6$ from R20F02, which falls in the NEQ regime. The examined centre locations are also visualized by the blue squares in figure 9 (b). Here, the local p.d.f. width is $W_p/D = 0.33$, and the local p.d.f. height is $H_p/D = 0.10$. The black lines indicate the same contour levels in the mean stationary profile $\overline{U}_s(y, z, t)$, and only 1 out of every 3 contour lines near the wake core are shown for clarity.

4.4. *Conditional averaging*

Due to the meandering of the wake, the deficit velocity profile $\overline{U}(y, z, t)$ is a blending of the stationary velocity profile $U_s(y, z, y_c, z_c, t)$ and the surrounding flow, i.e., constant zero velocity deficit, as in equation (2.6). The simplified superposition equation (2.11) requires self-similarity in the conditional stationary velocity. Here, we turn to examine the conditional stationary velocity profiles $U_s(y, z, y_c, z_c, t)$ obtained by conditional averaging on the centre location (y_c, z_c). In figure 13, the examined (y_c, z_c) pairs are offset from the mean wake centre in different directions, and the offset distance is comparable to the local width W_p and height H_p of the joint p.d.f. $p_c(y_c, z_c, t)$.

In figure 13 (e), when (y_c, z_c) is at the mean wake centre, $U_s(y, z, y_c, z_c, t)$ is Gaussian

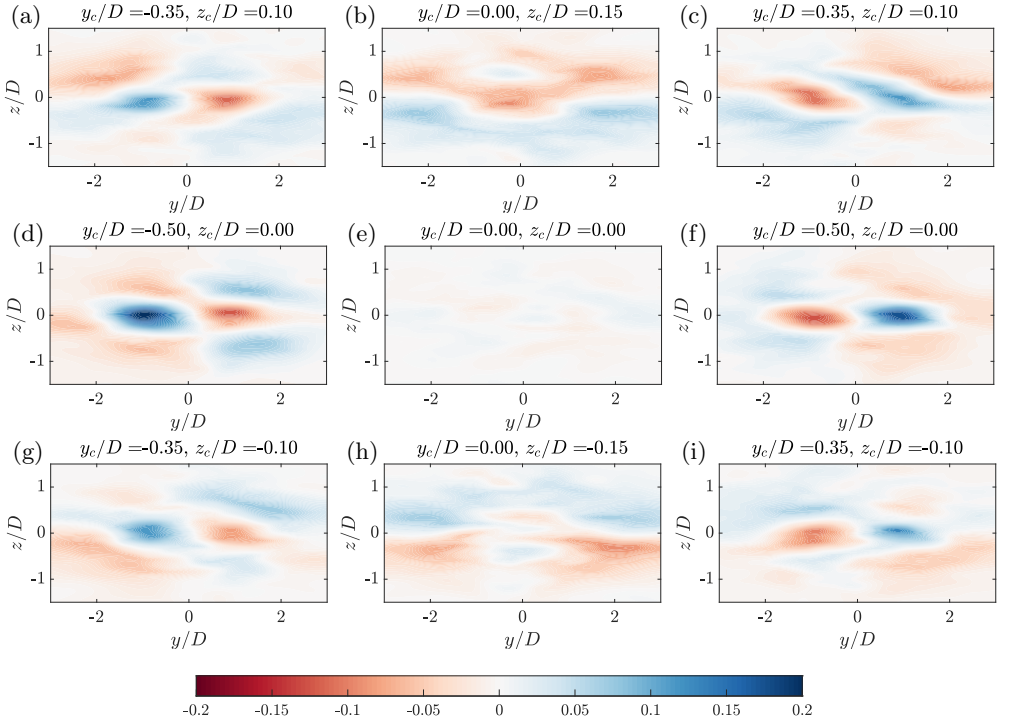

FIGURE 14. The difference $\Delta U_s/U_{s0}$ between the conditional stationary velocity $U_s(y, z, y_c, z_c, t)$ and the mean stationary velocity $\overline{U}_s(y, z, t)$, normalized by U_{s0}. The examined centre locations and the time step are the same as in figure 13. Here, the local p.d.f. width is $W_p/D = 0.33$, and the local p.d.f. height is $H_p/D = 0.10$.

like, and is almost the same as the mean stationary profile $\overline{U}_s(y, z, t)$. However, with (y_c, z_c) away from the mean wake core, $U_s(y, z, y_c, z_c, t)$ is distorted due to the meandering. In figures 13 (b,h), when (y_c, z_c) is offset from the mean wake centre in the vertical direction, $U_s(y, z, y_c, z_c, t)$ is still similar to the mean stationary profile $\overline{U}_s(y, z, t)$ near the mean wake core. When $y_c = 0, z_c > 0$, the wake meanders to the upper side of the domain, and thus the lower half of the profile $z < 0$ is near the mean wake core; We see a wider profile in the lower half of the wake in the periphery, and this is due to the stronger turbulence intensity in the mean wake core. When $y_c = 0, z_c < 0$, things are the opposite, and the upper half of the profile $z > 0$ is near the mean wake core; We see a wider profile in the upper half of the wake in the periphery, instead. In figures 13 (d,f), when (y_c, z_c) is offset from the mean wake centre in the horizontal direction, $U_s(y, z, y_c, z_c, t)$ is distorted both near the wake core and in the periphery. Similarly, when $y_c > 0, z_c = 0$, the conditional stationary profile is more vertically dispersed in the left half of the profile $y < 0$; When $y_c < 0, z_c = 0$, the conditional stationary profile is more vertically dispersed in the right half of the profile $y > 0$. In figures 13 (a,c,g,i), the distortion is the combination of the horizontal offset and the vertical offset. We observe that the distortion near the wake core is mainly in the horizontal direction while the distortion in the periphery is in both the vertical and the horizontal directions. The differences between the horizontal offset and the vertical offset indicate a stronger flow structure in the conditional stationary profile when with a horizontal offset.

In figure 14, we show the normalized difference $\Delta U_s/U_{s0}$ between the conditional stationary velocity $U_s(y, z, y_c, z_c, t)$ and its mean $\overline{U}_s(y, z, t)$. With the mean $\overline{U}_s(y, z, t)$

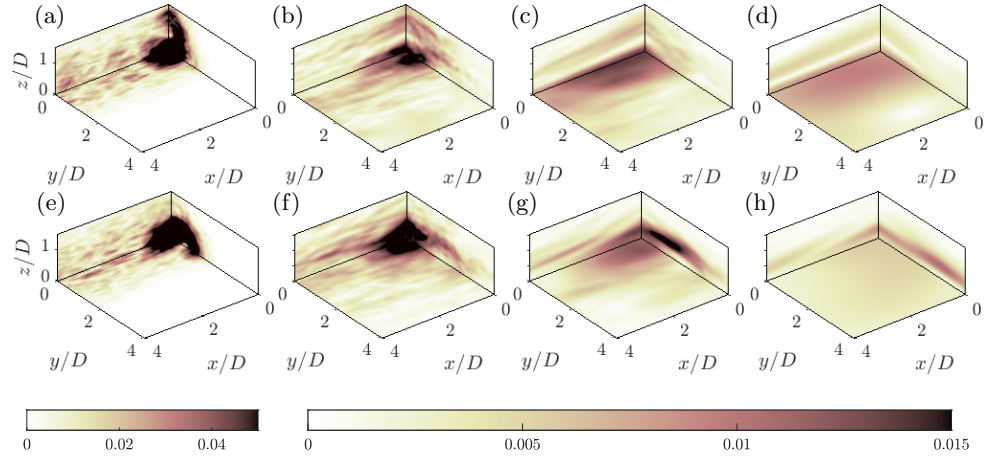

FIGURE 15. The vortex structures of the conditionally averaged three-dimensional flow field for case R20F10. The sampling points are from (a-d) $-W_p/3 \leqslant y_c < W_p/3$, $z_c \geqslant H_p/3$ and (e-h) $y_c > W_p/3$, $-H_p/3 \leqslant z_c < H_p/3$. The considered time steps are (a,e) $Nt = 1.4$, (b,f) $Nt = 12.9$, (c,g) $Nt = 29.3$, (d,h) $Nt = 100.0$. We show slices of the vorticity magnitude $|\omega|D/U_B$ at the centre planes $x = 0$, $y = 0$ and $z = 0$ respectively. The first column has thecolourmap $|\omega|D/U_B \in [0, 0.05]$, while the remaining columns have thecolourmap $|\omega|D/U_B \in [0, 0.015]$.

extracted, the difference field $\Delta U_s/U_{s0}$ shows the embedded large-scale structures. When there is a large horizontal offset $|y_c|/W_p = 1.5$ as in figure 14 (d,f), near the horizontal centreline $z = 0$, we see a high-velocity zone in $y > 0$ when $y_c > 0$ and $y < 0$ when $y_c < 0$, and a low-velocity zone in $y < 0$ when $y_c > 0$ and $y > 0$ when $y_c < 0$. Furthermore, away from the horizontal centreline $z \neq 0$, the pair of high-velocity and low-velocity zones switch sides, and thus the multiple pairs constitute vertically layered vortical structures in $\Delta U_s/U_{s0}$. However, when there is a large vertical offset $|z_c|/H_p = 1.5$ as in figure 14 (b,h), the pair of high-velocity and low-velocity zones are not as strong. When the centre location offset is a combination of $|y_c|/W_p = 1.0$ and $|z_c|/H_p = 1.0$ as in figure 14 (a,c,g,i), $\Delta U_s/U_{s0}$ is mainly layered vortical structures as the pure horizontal offset, with a small tilting of the pairs of high-velocity and low-velocity zones. According to equation (2.6), the pairs of high-velocity and low-velocity zones give rise to a bit fatter profile at the centrelines and a thicker tail in the vertical direction. Overall, the distortion in the conditional stationary velocity leads to the deviation of the mean stationary velocity $\overline{U}_s(y, z, t)$ from the Gaussian profile.

We visualize the vortical structures in the conditionally averaged three-dimensional flow field in figure 15. The conditional average is carried out for the centre location in a range to obtain more collapsed flow fields. The size of the vortical structure is comparable in the horizontal and vertical direction at the near wake regime. The vortical structure gradually extends in the horizontal directions and is suppressed in the vertical direction as in figures 15 (b,c,f,g). Note that the characteristic streamwise length is comparable to the characteristic spanwise length, and this is consistent with the observation of large horizontal vortical structures in the late wake (Lin & Pao 1979). In the end, the vortical structures develop strong vertical layering in figures 15 (d,h). We also compare the vorticity field between conditionally averaged on vertical offset, i.e., $-W_p/3 \leqslant y_c < W_p/3$, $z_c \geqslant H_p/3$, and on horizontal offset, i.e., $y_c > W_p/3$, $-H_p/3 \leqslant z_c < H_p/3$. We see the stronger horizontal gathering of the flow structures in the conditional average on horizontal offset in figures 15 (e-h). In figure 15 (h), it develops into layers of flow structures spanning even longer in y-direction than in x-direction. Therefore, we confirm

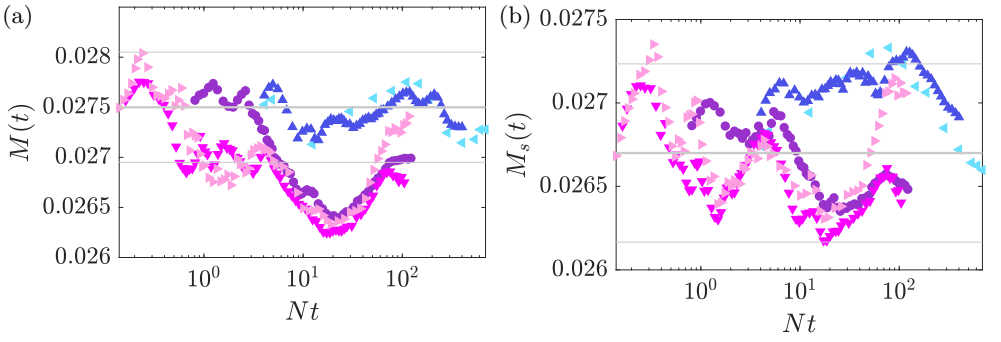

FIGURE 16. Verification of the conservative equations (a) for U, $M(t) = \text{const}$ and (b) for $\overline{U}_s$, $M_s(t) = \text{const}$. The initialization leads to the initial constant value of $M(t)$ to be $M_0 = 0.275$, indicated by the thick solid line in (a). The thin solid lines are where $102\%, 98\%$ of M_0 lie. Similarly in (b), we indicate the initial value of $M_s(t)$, i.e., $M_{s0} = 0.0267$ by the thick solid line, and $102\%, 98\%$ of M_{s0} by the thin solid lines. Thecolour and type of the symbols indicates different cases as defined in table 1.

the persistence of the large horizontal structures under the meandering effect, especially when the instantaneous flow has a horizontal offset. The existence of the large flow structures modifies the self-similarity and brings difficulties in measuring the meandering effect.

4.5. *Momentum flux*

Next, we verify the simplified momentum flux equations (2.18) and (2.19) for all the cases in figure 16. The nondimensional momentum flux $M(t) = U_0WH/U_BD^2$ stands within the range of $95\% \sim 102\%M_0$ for the mean velocity $\overline{U}(y,z,t)$ and $M_s(t) = U_{s0}W_sH_s/U_BD^2$ mostly within the range of $98\% \sim 102\%M_{s0}$ for the mean stationary velocity $\overline{U}_s(y,z,t)$. Here, $M_0 = 0.0275$ is the initial nondimensional momentum flux of $\overline{U}$ for all cases. For $\overline{U}_s$, the initial nondimensional momentum flux M_{s0} is around 0.0267.

The simplified conservation equations are based on the assumption $U_0 \ll U_B$ and the assumption of self-similarity in $\overline{U}$ and $\overline{U}_s$. In the near wake regime, all the cases see a relatively large variation in $M(t)$ and $M_s(t)$ since $U_0 \sim 0.1U_B$. Later, U_0 gradually decays to a relatively small value and the variation of $M(t)$ and $M_s(t)$ is smaller. However, as the deviation from the Gaussian profile grows, $M(t)$ and $M_s(t)$ go through a large variation again. Generally, the varying range of $M_s(t)$ is much smaller than the varying range of $M(t)$. Hence, the meandering behaviour is a factor of the momentum flux deviating from a constant, which is possibly due to its distorting self-similar profiles.

In the range of Re_B we examine, Re_B does not show its impact on $M(t)$ or $M_s(t)$ till the very late wake, as what we see near $Nt \sim \mathcal{O}(10^2)$ between R20F50 and R50F50 in both figures. This is consistent with the fact that the viscous force gradually becomes comparable to the inertial force and impacts the turbulent motions in the late wake (Billant & Chomaz 2001). The strength of background stratification is indicated by Fr_B, and it has a stronger impact than Re_B. In section 4.2, a small Fr_B case, e.g., R20F02, has a smaller discrepancy from the 2D Gaussian profile in the late wake. Therefore, a smaller variation in $M(t)$ and $M_s(t)$ is also observed for low Fr_B cases.

In general, the nondimensional momentum flux, $M(t)$ and $M_s(t)$, can be seen as a constant through the wake development. Using the momentum flux from the stationary velocity $M_s(t)$ with low Fr_B and high Re_B maximizes the accuracy of that constant. The momentum flux equations bridge the scaling of the velocity deficit U_0 and the scaling of the length scales W, H (Meunier *et al.* 2006). Note that the momentum flux equations

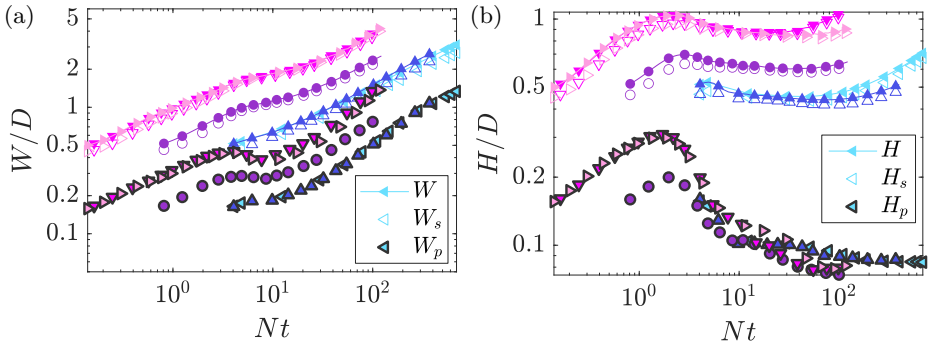

FIGURE 17. The development of the width and the height. The solid symbols on a solid line are the width and the height of the mean velocity profiles $\overline{U}$, the hollow symbols are for the mean stationary velocity $\overline{U}_s$, and the solid symbols with a black outline are for centre location p.d.f. p_c. Thecolour and type of the symbols indicates different cases as defined in table 1. Note that all the cases except R10F02 show the symbols every 4 points for clarity.

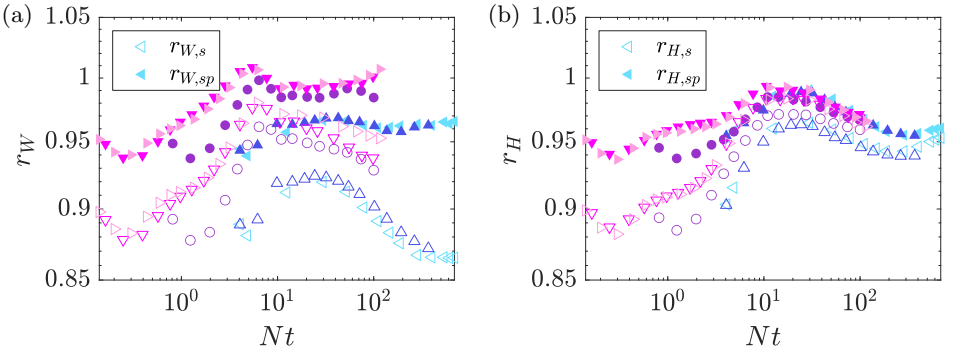

FIGURE 18. The ratio of (a) the widths and (b) the heights between different length scales. The hollow symbols are for $r_{W/H,s}$ and the solid symbols are for $r_{W/H,sp}$, as defined in equations (4.1). Thecolour and type of the symbols indicates different cases as defined in table 1. Note that all the cases except R10F02 show the symbols every 4 points for clarity.

(2.18) and (2.19) are obtained based on only two assumptions, and they may also stand in other wakes as long as we have $U_0 \ll U_B$ and a roughly correct self-similarity.

4.6. *Superposition of the meandering effect*

Now, we examine the meandering effect in the statistics scaling. The meandering effect, quantified by $p_c(y_c, z_c, t)$, can be superposed on the conditional stationary velocity $U_s(y, z, y_c, z_c, t)$ as in equation (2.6).

According to equation (2.14), the characteristic length scales of the mean profile W, H can be the superposition of the length scales of the mean stationary profile W_s, H_s and the length scales of the centre location p.d.f. W_p, H_p. In figure 17, the development of multiple widths and heights are shown. The widths of the stationary velocity W_s and the meandering range W_p are constantly growing, while each has three stages with different growth rates. A clear plateau exists in the meandering width W_p for all cases, indicating a sudden period of suppression in the meandering behaviour. Similarly, the height of the stationary velocity H_s grows at the beginning and at the end of the flow, while it also plateaus in between. Compared to the width, the first transition of the height H_s scaling is a lot earlier and the following regime of constant height lasts longer, and the growth in all three regimes is generally at a slower rate. Unlike H_s, the height of the meandering

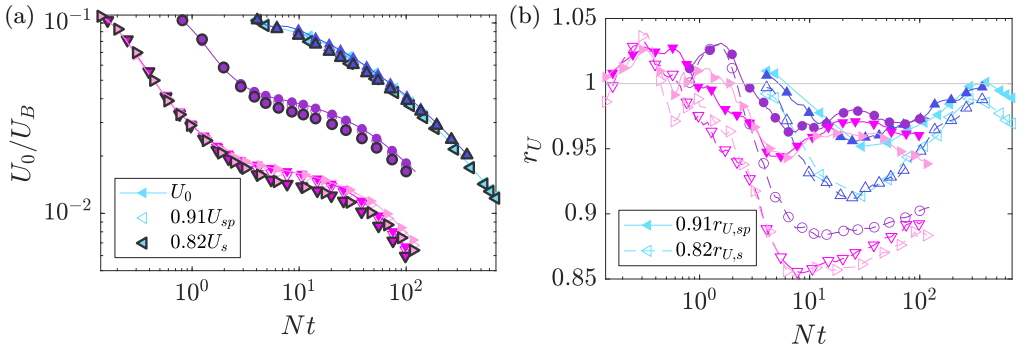

FIGURE 19. (a) The development of the velocity deficit. The solid symbols on a solid line are the mean velocity deficit U_0. The hollow symbols are proportional to the superposed velocity $U_{sp0} \equiv M_0/W_{sp}H_{sp}$, obtained from the momentum flux equation, and 0.91 is the initial value of U_0/U_{sp0}. The solid symbols with a black outline are proportional to the mean stationary velocity U_{s0}, where 0.82 is the initial value of U_0/U_{s0}. (b) The ratio between the velocity deficits, $r_{U,s}$ and $r_{U,sp}$, as defined in equation (4.2). Thecolour and type of the symbols indicates different cases as defined in table 1. Note that all the cases except R10F02 show the symbols every 4 points for clarity.

range H_p grows at the beginning, then decays fast for a short period and decays slowly for a long period until it gradually approaches a constant in the late wake. The diverse scaling behaviour suggests multiple critical points in the length scales W_s, W_p, H_s, H_p, because the buoyancy impact is gradually changing through the wake. Therefore, the transition points of the four characteristic length scales are not necessarily the same as each other.

The five cases share the three-regime behaviour in length scales, though the transition points are vague to identify. Also, the growth rates in the same regime are close to each other (Meunier *et al.* 2006). In the range of Re_B we examined, Re_B has a minor impact on the widths W_s and W_p through the wake. Meanwhile, the heights H_s and H_p do not change with Re_B at the beginning, while low Re_B increases the height H_s greatly in the late wake, which further verifies the importance of the viscous force in the late wake scaling. The background Froude number Fr_B changes the length scale magnitude greatly. With stronger background stratification, i.e., low Fr_B, the length scales will get earlier affected by the buoyancy, and thus, they usually are a lot smaller at the same $Nt = Fr_B^{-1} \cdot \bar{x}/D$.

In figure 18, we show the length scale ratios

$$r_{W,s} = W_s/W,\ r_{W,sp} = W_{sp}/W, \quad r_{H,s} = H_s/H,\ r_{H,sp} = H_{sp}/H. \tag{4.1}$$

The superposed width and height given by equation (2.14) fall close to the mean wake width and height. Since the range of the meandering is around 1/3 of the mean wake size, the change of the width and height due to the superposition of the meandering will be around 5%. The rest of the discrepancy shall be attributed to the distortion of the wake profiles. We observe that the meandering has a consistent impact on the wake width, but a reducing impact on the wake height due to the reducing vertical meandering.

On the other hand, we also want to learn about the impact of the meandering on the characteristic velocity scale. The simplified superposition equation (2.11) will lead us to the analytical expression of the self-similar velocity profile, if not considering the distortion of the conditional velocity profile $U_s(y, z, y_c, z_c, t)$ due to the large flow structures under a horizontal meandering. We examined the two-dimensional Gaussian assumption of the mean stationary velocity in section 4.2 and of the centre location p.d.f.

in section 4.3. In equation (2.13), the mean velocity deficit $U_0(t)$ can be simplified to be proportional to the mean stationary deficit $U_{s0}(t)$. The mean velocity deficit $U_0(t)$ can also be obtained utilizing the momentum flux equation (2.18). In figure 19, we show the two ways to incorporate the meandering effect in the velocity deficit, and the velocity ratios

$$\begin{aligned} r_{U,s} &= U_{s0}/U_0, \\ r_{U,sp} &= U_{sp0}/U_0, \quad \text{where } U_{sp0} = M_0/W_{sp}H_{sp}. \end{aligned} \tag{4.2}$$

The meandering effect does not necessarily bring a constant shift according to $r_{U,s}$, though the meandering length scales W_p, H_p share a generally similar trend as the mean stationary length scales W_s, H_s. Such a naive assumption of a constant shift will lead to up to 15% error, especially in the late wake regime due to the accumulation of the error. By using the momentum flux equation, the meandering effect on the velocity deficit is considered as a direct outcome of expanding width and height due to the meandering dispersion. The normalized superposed velocity $U_{sp0}(t)$ has less than 5% discrepancy. In fact, the proportional relationship (2.13) can turn to the same form of $U_{sp0}(t)$ using Gaussian profiles, and we leave out the derivation for brevity. Therefore, assuming constant in the proportionality (2.13) is a further simplified version of $U_{sp0}(t)$, and is expected to have lower accuracy in understanding meandering.

The mean velocity deficit $U_0(t)$ in all cases shows a general three-stage behaviour. In the near wake regime, the velocity decays fast, and gradually transitions to a lower decay rate as the buoyancy effect builds up its influence, while in the vertically collapsed late wake regime, the velocity decays fast again. Though the decay rates are similar among cases, the transition points are vague to identify due to the gradual change. From the view of characteristic length scales, the width and the height are experiencing the transitions at different Nt since the flow develops anisotropy in a stratified environment. This leads to further intricacy in the velocity scaling. Though Fr_B only affects the intercept of a power law scaling, Re_B brings a subtle change of the decay rate in the late wake. Therefore, it is reasonable to see that more regimes are discovered apart from the three regimes, i.e., the NW, the NEQ and the Q2D regimes, and that the decay rates differ between cases (Brucker & Sarkar 2010; Bonnier & Eiff 2002). A more delicate velocity scaling law with more than three stages is possible. Due to the robustness of the momentum flux equation, the consideration of possible stages in characteristic lengths will assist in understanding the velocity. The utilization of length scales also directly provides physical insights into the turbulent motion evolution.

5. Conclusion

Large horizontal structures accompanied by the suppression of the vertical motions are widely observed in the stratified environment. As a canonical case, a stratified wake of a sphere has the large horizontal structures emerging in the late wake. However, the growing meandering effects on the wake statistics are seldom considered. In this work, we study the meandering behaviour by examining $\mathcal{O}(100)$ DNSs, which cover Re_B in $[10\,000, 50\,000]$ and Fr_B in $[2, 50]$. We decompose the instantaneous velocity into the stationary velocity and the centre location meandering.

The horizontal meandering range constantly grows as the stationary profile width does, while the vertical meandering range grows at the beginning and reduces to a constant in the late wake, which is in contrast with the slowly growing stationary profile height. In general, the range of meandering is much smaller than the wake profile size. Therefore, the existence of meandering leads to around 5% change in the wake length scales according

to the superposition equations, and for the wake height, the meandering effect becomes more insignificant due to the buoyancy suppression.

During the process of meandering, the velocity profile gradually deviates from the self-similar Gaussian profile. The conditional velocity will be dispersed accordingly based on the meandering direction, and thus the mean wake profile grows larger. A horizontal centre location offset will lead to a large local horizontal structure, while a vertical offset will not. Also, the suppression of the vertical meandering is further related to the suppression of the variation in the instantaneous wake height, while the instantaneous wake width still has a large variation range. Such differences result in the distortion of the velocity profile, and thus the mean profile deviates from the self-similarity assumption. Isolating the stationary velocity from the meandering behaviour achieves a better self-similarity. According to our theoretical analysis, based on the self-similarity assumption, the nondimensional momentum flux is nearly constant through the wake. We verified the constant flux behaviour for all the cases, and the momentum flux of the stationary profile without meandering is closer to a constant as expected.

In the meantime, the momentum flux equation bridges the scaling of the velocity deficit and the scaling of the wake lengths. The results suggest a varying meandering effect on the scaling of the velocity deficit though the meandering range is comparably small and does not alter the width and height significantly. A simple proportionality to the stationary velocity deficit oversimplifies the meandering effect and brings a large discrepancy between the velocity superposed with the meandering and the mean velocity deficit. To understand this discrepancy, we examine the length scales, as inspired by the momentum flux equation. We find the three-stage behaviour in both the width and the height while the transition points between stages are fairly different from each other. This brings intricacy to the velocity scaling. In contrast, the scaling of the superposed velocity obtained from the superposed length scales shows a much smaller discrepancy from the mean velocity deficit. Therefore, we conjecture that the scaling of the velocity deficit can be better understood by the combination of the width and the height. The width and the height do not share the critical transition points and thus the velocity scaling will be more complicated than three stages.

Our results show that Re_B does not come into effect till the late wake, where the viscous force starts to play a role against the buoyancy. The background stratification Fr_B directly determines the entering of the buoyancy and thus changes the intercept of the scaling greatly. Small Fr_B has a stronger suppression on the vertical motion, especially the vertical meandering range, and also the variation range of the wake height. Further efforts are required to find the quantified dependence on the Re number and the Fr number.

Acknowledgement

This work is supported by ONR grant no. N000142012315, and the computation is conducted on Penn State Roar system. The authors would like to thank Dr. Xiang I.A. Yang for the fruitful discussion on the results, and Dr. Mogeng Li for the technical supports for the visualization and the discussion on the results.

REFERENCES

Antonia, RA 1981 Conditional sampling in turbulence measurement. *Ann. Rev. Fluid Mech.* **13** (1), 131–156.

Basak, Sankarananda & Sarkar, S 2006 Dynamics of a stratified shear layer with horizontal shear. *J. Fluid Mech.* **568**, 19.

Billant, Paul & Chomaz, Jean-Marc 2001 Self-similarity of strongly stratified inviscid flows. *Phys. Fluids* **13** (6), 1645–1651.

Bonnier, Marion & Eiff, Olivier 2002 Experimental investigation of the collapse of a turbulent wake in a stably stratified fluid. *Phys. Fluids* **14** (2), 791–801.

Botev, Zdravko I, Grotowski, Joseph F & Kroese, Dirk P 2010 Kernel density estimation via diffusion. *The annals of Statistics* **38** (5), 2916–2957.

Brucker, Kyle A & Sarkar, Sutanu 2010 A comparative study of self-propelled and towed wakes in a stratified fluid. *J. Fluid Mech.* **652**, 373–404.

de Bruyn Kops, Stephen M & Riley, James J 2019 The effects of stable stratification on the decay of initially isotropic homogeneous turbulence. *J. Fluid Mech.* **860**, 787–821.

Chongsiripinyo, Karu & Sarkar, Sutanu 2020 Decay of turbulent wakes behind a disk in homogeneous and stratified fluids. *J. Fluid Mech.* **885**.

Diamessis, Peter J, Spedding, Geoffrey R & Domaradzki, J Andrzej 2011 Similarity scaling and vorticity structure in high-reynolds-number stably stratified turbulent wakes. *J. Fluid Mech.* **671**, 52–95.

Dommermuth, Douglas G, Rottman, James W, Innis, George E & Novikov, Evgeny A 2002 Numerical simulation of the wake of a towed sphere in a weakly stratified fluid. *J. Fluid Mech.* **473**, 83–101.

Gourlay, Michael J, Arendt, SC, Fritts, DC & Werne, J 2001 Numerical modeling of initially turbulent wakes with net momentum. *Physics of Fluids* **13** (12), 3783–3802.

Hopfinger, EJ 1987 Turbulence in stratified fluids: A review. *Journal of Geophysical Research: Oceans* **92** (C5), 5287–5303.

Keck, Rolf-Erik, de Maré, Martin, Churchfield, Matthew J, Lee, Sang, Larsen, Gunner & Aagaard Madsen, Helge 2014 On atmospheric stability in the dynamic wake meandering model. *Wind Energy* **17** (11), 1689–1710.

Kim, John, Moin, Parviz & Moser, Robert 1987 Turbulence statistics in fully developed channel flow at low Reynolds number. *J. Fluid Mech.* **177**, 133–166.

Krug, Dominik, Philip, Jimmy & Marusic, Ivan 2017 Revisiting the law of the wake in wall turbulence. *Journal of Fluid Mechanics* **811**, 421–435.

Li, Junyi & Yang, Yantao 2021 Thermohaline interleaving induced by horizontal temperature and salinity gradients from above. *Journal of Fluid Mechanics* **927**.

Li, Mogeng, de Silva, Charitha M, Chung, Daniel, Pullin, Dale I, Marusic, Ivan & Hutchins, Nicholas 2021 Experimental study of a turbulent boundary layer with a rough-to-smooth change in surface conditions at high reynolds numbers. *Journal of Fluid Mechanics* **923**.

Lin, Jung-Tai & Pao, Yih-Ho 1979 Wakes in stratified fluids. *Ann. Rev. Fluid Mech.* **11** (1), 317–338.

Mahrt, Larry 1999 Stratified atmospheric boundary layers. *Boundary-Layer Meteorol.* **90** (3), 375–396.

Meunier, Patrice, Diamessis, Peter J & Spedding, Geoffrey R 2006 Self-preservation in stratified momentum wakes. *Phys. Fluids* **18** (10), 106601.

Nedić, J, Vassilicos, John Christos & Ganapathisubramani, Bharathram 2013 Axisymmetric turbulent wakes with new nonequilibrium similarity scalings. *Physical review letters* **111** (14), 144503.

Nidhan, Sheel, Schmidt, Oliver T & Sarkar, Sutanu 2021 Coherence in turbulent stratified wakes deduced using spectral proper orthogonal decomposition. *arXiv preprint arXiv:2105.06656* .

Pal, Anikesh, Sarkar, Sutanu, Posa, Antonio & Balaras, Elias 2017 Direct numerical simulation of stratified flow past a sphere at a subcritical reynolds number of 3700 and moderate froude number. *J. Fluid Mech.* **826**, 5–31.

Pope, SB 2000 *Turbulent Flows*. Cambridge University Press.

Rowe, KL, Diamessis, PJ & Zhou, Q 2020 Internal gravity wave radiation from a stratified turbulent wake. *J. Fluid Mech.* **888**.

Smyth, William D & Moum, James N 2000 Length scales of turbulence in stably stratified mixing layers. *Phys. Fluids* **12** (6), 1327–1342.

Spedding, GR 1997 The evolution of initially turbulent bluff-body wakes at high internal froude number. *J. Fluid Mech.* **337**, 283–301.

Spedding, GR 2001 Anisotropy in turbulence profiles of stratified wakes. *Phys. Fluids* **13** (8), 2361–2372.

Spedding, GR 2002*a* The streamwise spacing of adjacent coherent structures in stratified wakes. *Phys. Fluids* **14** (11), 3820–3828.

Spedding, GR 2002*b* Vertical structure in stratified wakes with high initial froude number. *J. Fluid Mech.* **454**, 71–112.

Spedding, GR, Browand, FK & Fincham, AM 1996 Turbulence, similarity scaling and vortex geometry in the wake of a towed sphere in a stably stratified fluid. *J. Fluid Mech.* **314**, 53–103.

de Stadler, Matthew B & Sarkar, Sutanu 2012 Simulation of a propelled wake with moderate excess momentum in a stratified fluid. *J. Fluid Mech.* **692**, 28–52.

de Stadler, Matthew B, Sarkar, Sutanu & Brucker, Kyle A 2010 Effect of the prandtl number on a stratified turbulent wake. *Phys. Fluids* **22** (9), 095102.

Tennekes, Hendrik, Lumley, John Leask, Lumley, Jonh L & others 1972 *A first course in turbulence*. MIT press.

Xiang, Xinjiang, Chen, Kevin K & Spedding, Geoffrey R 2017 Dynamic mode decomposition for estimating vortices and lee waves in a stratified wake. *Exp. Fluids* **58** (5), 1–10.

Yang, Xiaolei & Sotiropoulos, Fotis 2019 A review on the meandering of wind turbine wakes. *Energies* **12** (24), 4725.

Yang, Yantao, Chen, Wenyuan, Verzicco, Roberto & Lohse, Detlef 2020 Multiple states and transport properties of double-diffusive convection turbulence. *Proceedings of the National Academy of Sciences* **117** (26), 14676–14681.

Yang, Yantao, Van Der Poel, Erwin P, Ostilla-Mónico, Rodolfo, Sun, Chao, Verzicco, Roberto, Grossmann, Siegfried & Lohse, Detlef 2015 Salinity transfer in bounded double diffusive convection. *J. Fluid Mech.* **768**, 476–491.

Zhou, Qi & Diamessis, Peter J 2016 Surface manifestation of internal waves emitted by submerged localized stratified turbulence. *J. Fluid Mech.* **798**, 505–539.